Flight-Experiment Validation of the Dynamic Capabilities of a Flux-Pinned Interface as a Docking Mechanism

Frances Zhu
Cornell University
452 Upson Hall
Ithaca, NY 14853
913-777-9595
fz55@cornell.edu

Mitchell Dominguez
Cornell University
Ithaca, NY 14853
md697@cornell.edu

Mason Peck
Cornell University
455 Upson Hall
Ithaca, NY 14853
607-255-4023
Mp336@cornell.edu

Laura Jones-Wilson
Jet Propulsion Laboratory,
California Institute of Technology
4800 Oak Grove Dr.
Pasadena, CA 91109
Laura.L.Jones@jpl.nasa.gov

***Abstract*—Flux-pinned interfaces for spacecraft leverage the physics of superconductor interactions with electromagnetism to govern the dynamics between two bodies in close-proximity. Several unique advantages over traditional mechanical capture systems include robustness to control failures, contactless reorientation of the capture target, and collision mitigation. This study describes a series of experiments performed in a microgravity environment during a parabolic-flight campaign to measure the dynamic behavior of a flux-pinned interface in a flight-traceable environment. This paper presents the performance of a flux-pinned interface in the full six degrees of freedom in terms of several quantifiable metrics: success of capture at various energetic states, momentum change, system damping, and interface stiffness of the two spacecraft bodies.**

TABLE OF CONTENTS

1. INTRODUCTION 1
2. BACKGROUND 2
3. METHODOLOGY 2
4. DYNAMIC METRICS 5
5. DYNAMICS CAPABILITIES 6
6. CONCLUSIONS 11
REFERENCES 12
BIOGRAPHY 13
APPENDIX ...... ERROR! BOOKMARK NOT DEFINED.

1. INTRODUCTION

Flux-pinning physics can generate a stable, stiff joint between two bodies whose motion is characterized by up to six degrees of freedom without mechanical contact or active control. The dynamic behavior of such interfaces has many applications for manipulating spacecraft relative motion, including self-assembly, reconfiguration, station-keeping, and formation flying [1] [2] [3]. This paper focuses on utilizing a flux-pinned interface (FPI) as a docking interface in the context of a potential Mars Sample Return (MSR) mission [4]. A flux-pinned interface offers many advantages over conventional mechanical docking solutions [5]. In particular, contactless interaction reduces risk of damaging the spacecraft through collision mitigation [6]. The passivity and the stability of flux-pinned interfaces reduce the sensing and actuation requirements but necessitates more stringent thermal requirements on the spacecraft system to cryogenically cool the superconductors [7] [8]. Electromagnetic actuators can further enhance an FPI by enabling contactless manipulation during close-proximity maneuvers [9].

Flux-pinning technology has not yet been used in space. To reach a level of maturity such that it can be used in a flight mission, designers require a parametric mapping to system behavior and a predictive, reliable dynamics model. Recent research efforts have focused on developing a parametric mapping and predictive dynamics model [10] [11]. Numerous ground testbeds explore the capabilities of flux-pinned interfaces for several close-proximity spacecraft applications [12] [13]. These testbeds collect dynamic data under a multitude of initial conditions to aid characterization and development of a more predictive dynamics model. Due to the highly nonlinear coupled dynamics of flux-pinning physics, ground testing cannot fully assess, and thus does not accurately predict, the capabilities of a flux-pinned interface in a six degree-of-freedom environment [4]. A microgravity testbed enables the full expression of the coupled dynamics and better represents the capabilities in a spaceflight environment.

Parabolic flights enabled the collection of dynamic data from a fluxed pinned interface. Although parabolic flights offer only short periods of microgravity environment, data collected from these experiments offer highly relevant insight into the dynamics of an FPI in a space system [14] [15]. This suite of efforts steadily increases the technology readiness level of FPIs towards spaceflight adoption and implementation.

This paper reports the capabilities of an FPI configuration designed around a docking application. Section 2 discusses the basic physics behind flux-pinning technology and its implications for a spacecraft docking mechanism. Section 3 lists the relevant metrics that encapsulate the performance of the docking interface and the desired capabilities for a potential Mars Sample Return mission. Section 4 describes the experiment campaign, testbed design, and microgravity

978-1-5386-6854-2/19/$31.00 ©2019 IEEE

operations. Section 5 summarizes the observed capabilities of the docking interface from the microgravity experiment sensor data. Section 6 concludes the paper with mission implications and future work.

2. BACKGROUND

Flux pinning is an interaction between a magnetic source and type-II superconductors. A superconductor retains or “memorizes” the distribution of magnetic field within its volume when the temperature of the superconductor transitions below its material-dependent critical temperature. When a magnetic field is “field-cooled” into the superconductor, the superconductor resists changes in the magnetic field distribution by generating restorative forces and moments to bring the magnetic field source back to its field-cooled position and attitude, or state. With the presence of damping, flux-pinning dynamics ultimately allows a magnet to return to its equilibrium position and attitude, equivalent to the lowest energy state in the potential well created by the field-cooled superconductor [16] [7]. The edge of the magnetic potential well is the practical limit in which flux-pinning physics dominates all other physics, like friction, drag, or solar radiation pressure.

The field-cooled (FC) state has a significant effect on dynamic behavior and is only one of numerous critical design parameters. Firstly, the FC state initializes the natural equilibrium location for any magnet with the same properties as the field-cooling source. Multiple equilibria may exist for identical magnetic sources populating a single body– a concept utilized in this work. Secondly, the FC state also determines the stiffness of the interface by dictating the amount of captured magnetic flux in the superconductor that can respond to magnetic motion. Finally, the FC state determines the clearance distance between the two bodies moving relative to one another, which influences the amount of energy needed to force contact between them. Recent work describing parameter design to system level behavior, including but not limited to the FC state, can be found in reference [11].

The behavior of the interface after field cooling, under some simplifying assumptions, can be modeled by Kordyuk’s frozen image model and Villani’s dipole equations [17]. The frozen image model maps the magnetic field source to virtual images within the superconductor volume that interact with the source contactlessly [18]. The contactless nature of the interface implies that the mechanical interfacing/physical configuration do not directly influence the system’s behavior; rather, the magnetic field shape relative to the field-cooled magnetic source dominates the system behavior. The dynamics of the system is then primarily governed by an electrodynamical model derived by Villani et. al, which provides functions for force and torque given the spatial state and magnetic moment dipoles of two sources [19] [20].

The governing equations of motion show that the force and torque relationships are highly nonlinear and coupled. The nonlinearity varies stiffness as a function of spatial displacement r with an inverse polynomial order. The nonlinearity in the direction normal to the superconductor face produces desirable behaviors by offering collision mitigation forces between spacecraft. As the spacecraft passes the equilibrium FC position and nears contact, the flux-pinned interface acts to repel the incoming spacecraft with an increasing resistance force. The coupling of the degrees of freedom results in the attitude affecting imparted forces, and the position affecting imparted torques, enabling energy transfer across degrees of freedom (DOF). Observations made in a constrained-DOF environment will under-predict the performance of the FPI for a space-based system because the energy that would normally be distributed across all DOF become concentrated into the remaining unconstrained DOF. Furthermore, the depth of the potential well generated from field-cooling a magnetic source is not of equal shape and depth in each DOF due to asymmetries in the magnetic field source. Thus, the maximum energy that the system can absorb to successfully execute a capture maneuver differs across DOF.

This paper aims to expand upon the past work by conducting tests in microgravity, enabling the full coupled and nonlinear dynamics to be captured. The resulting data is used to inform a more accurate mapping between dynamic conditions and capture performance. Although outside the scope of this paper, the sensor data can be extended to inform a more general mapping of FPI performance and refine a predictive dynamics model.

3. METHODOLOGY

FPI Design Concept for Sample Capture Application

This work examines the relevant dynamic metrics of an FPI designed to capture a notional spherical orbiting sample cache (OS) that is a maximum of 12.5 kg [21]. For this proposed flux-pinning application, 12 magnets were mounted on the surface of the orbiting sample evenly on the perimeter of the 20.3 cm diameter sphere. The sample cache is much smaller than the return vehicle. Mass estimates for different flight-like sample capture and docking FPI designs can be found in reference [22].

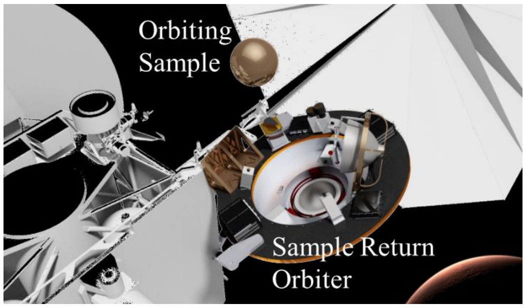

Figure 1: Spaceflight configuration considered to accommodate flux-pinned interface, Credit: NASA

The flux-pinned interface is passive, so no sensors or actuators are on the OS. The sample return orbiter (SRO), the other side of the interface, holds three superconductors and the peripheral thermal support flight components described in reference [23]. The SRO, also known as the return vehicle, maneuvers freely so that the capture plane, defined in Figure 2, is located at the edge of the magnetic potential well and normal to the boresight axis. The boresight axis originates from the center of the capture interface on the SRO and continues radially outward.

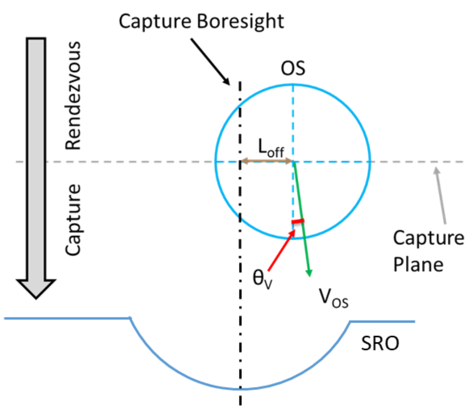

Figure 2: Variables associated with initial conditions in capture phase, listed in Table 1

Table 1 lists the initial conditions of OS's dynamic state the docking interface must be able to tolerate and still capture once the SRO is in place to capture. Figure 2 depicts the variables spatially as the orbiting sample enters the capture/docking phase of spaceflight operations.

Table 1: Initial Conditions in Capture Phase

Initial Condition	Value
Relative spin rate magnitude	$\left[\frac{\pi}{30}\ \frac{\pi}{10}\right]$ rad/s
Maximum lateral offset of the OS at the capture plane (L_{off})	0.1 m in any direction off the capture boresight axis
Velocity magnitude (V_{OS}) of the OS at the capture plane	[0.02 0.10] m/s
Maximum radial component of velocity results in max angle θ_V	5° in any radial direction

Testbed Design

For the microgravity experiments, the main test equipment consists of the orbiting sample analogue (OSA), seen in Figure 4 and sample return orbiter analogue (SROA), shown in Figure 5. These two components interact via a flux-pinned interface as shown in Figure 3.

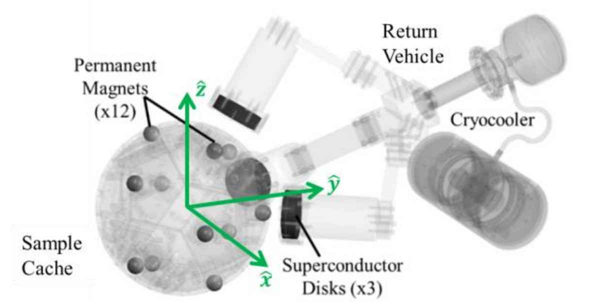

Figure 3: Multiple magnet and multiple superconductor flux-pinned docking interface concept with relative coordinate frame definition

The OS analogue is a spherical spacecraft analogue that holds 12 permanent magnets equidistant from the center of the sphere with the dipoles pointing radially outward. The permanent magnets are the magnetic sources that field-cool to their counterpart superconductors, creating and enabling flux-pinning physics during capture. The OSA has a diameter of 0.203 m, a mass of 2.5kg and a near-spherical inertia. The OSA's dimensions are to scale with the notional orbiting sample design. The OSA contains a sensor package and unique April tags are added to the surface, as shown in Fig. 4, both of which enable the dynamic state of the OSA to be computed [24]. These elements would not be required on a flight system. The sensor package within the OSA structure contains an IMU (gyroscope and accelerometer), which measures elements of the dynamic state, a computer, which logs the data, and a wireless transmitter, which sends the data to an accessible monitor.

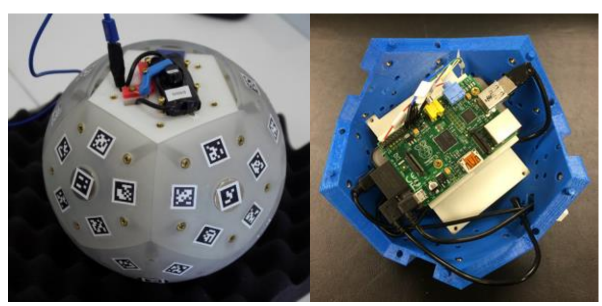

Figure 4: Left: surface of OSA populated with April tags. Right: sensor package inside OSA structure to support experiment

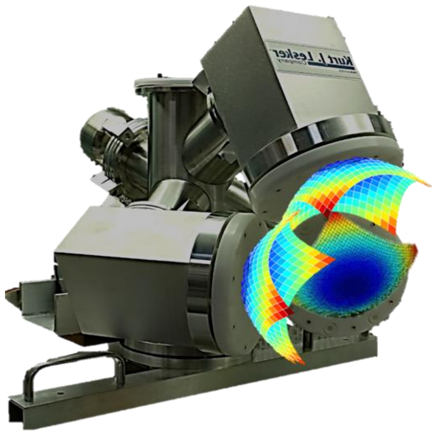

Figure 5: Magnetic potential wells above superconductor surfaces to conceptually depict interface potential well

The other half of the flux-pinned interface lies within the sample return orbiter analogue (SROA). Three superconductors [25] reside within a vacuum chamber with a cryocooler that cools and maintains the superconductors below the material's critical temperature. The thermal subsystem that enables flux-pinning technology has built-in fault tolerance, of which the design and testing is fully described in [23]. The cryocooling system is flight-traceable and the vacuum chamber is additional equipment needed for testing on Earth. Figure 5 shows SROA system and a conceptual magnetic potential well that the superconductors sustain. As with the OSA, the surface of the SROA has unique April tags and an IMU mounted close to the docking interface surface. The April tags offer static reference markers to generate the OSA's position and attitude relative to the SROA. The SROA IMU provides reference motion in the frame that the OSA's motion operates within. The dynamic sensors are circled and labeled in Figure 6.

The SROA is mounted to an integrated frame assembly (IFA) that contains SROA support equipment, a launching mechanism, tracking cameras, and handling features for the experimenters, shown in Figure 6. The launching mechanism consists of two variable speed motors that can be driven independently and belt assemblies that grip the OSA to impart initial conditions every time the OSA is fed into the assembly. The IFA also hosts five GoPro cameras that collect video footage that is post-processed to determine the FPI dynamics. A laptop on the IFA collects all sensor data and controls the launching mechanism. The IFA is only connected to the aircraft by a long power cord and a safety tether designed to be as flexible as possible to avoid imposing undesired torques on the free-floating frame.

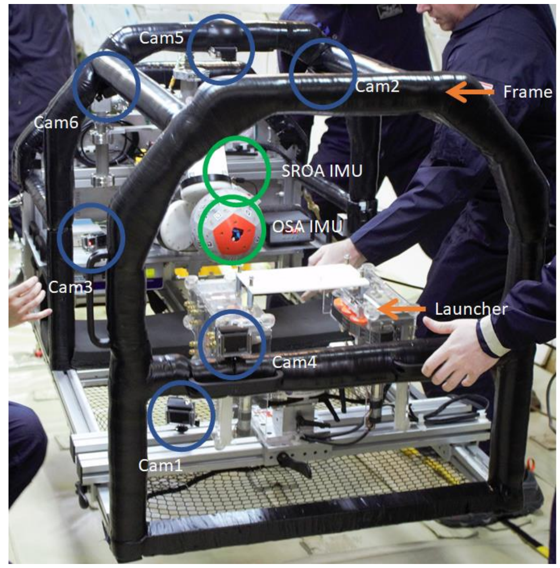

Figure 6: Dynamic sensors on experiment testbed; cameras circled in blue and IMU's in green

Experiment Campaign

To measure the metrics of interest, the two spacecraft analogues incorporating an FPI were tested in a microgravity environment. Two types of experiments were conducted: capture experiments and equilibrium experiments.

The capture experiments initialize the spacecraft analogues outside the magnetic potential well in the capture plane with a range of translational and angular velocities (energetic boundaries found in prior ground testing). The capture experiments aim to characterize the boundary between capture and no capture outcomes, identifying the range of initial conditions that lead to successful capture. The equilibrium experiments, on the other hand, initialize the relative state of the spacecraft analogues within their established magnetic potential well near the equilibrium state to characterize the near-equilibrium stiffness and damping effects.

Microgravity Operations

This paper discusses results from a March 2018 microgravity aircraft flight campaign, which consisted of 50 parabolic maneuvers over the course of two days. Each parabola provides a microgravity environment for ~30 seconds in which dynamic data is collected continuously for the entire duration of the flight. At the start of each parabola, the IFA is positioned in the middle of the allocated aircraft experiment area, the OSA is positioned into its initial position, and the experimenters release the frame, as shown in Figure 7. Environmental factors during operation can lead to disturbances (such as contact with the aircraft or experimenters) on the OSA-SROA system. When such a contact is noted the experiment is reset with a new free-float trial in the same parabola. Each trial is considered a separate experiment for this paper. This process is continued until the end of the free-float period and the experiment is placed on the aircraft deck to wait until the next microgravity phase.

Figure 7: Experiment setup for a capture experiment

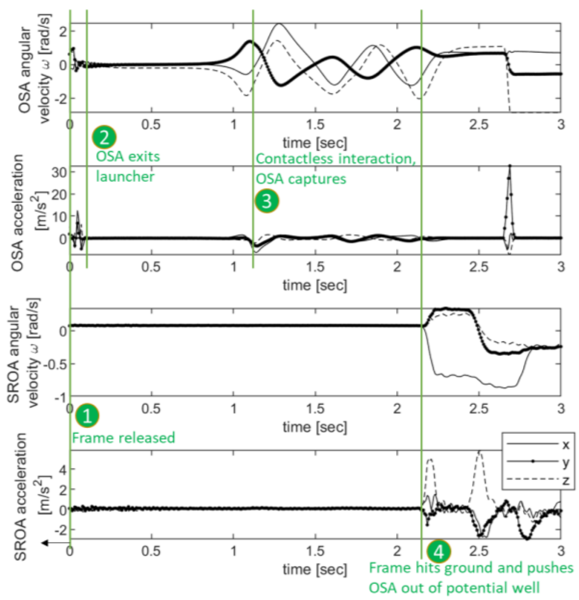

Figure 8: Sample of IMU data with sequential events labeled

A sample of IMU data from the experiment is detailed with reference events in Figure 8. Progressing in chronological order, the frame is first released with minimal motion (1). The frame's angular velocity is minimal, and acceleration is near zero. During release, the OSA rattles in the launcher seen in the OSA's IMU measurements prior to exiting the launcher. The OSA leaves the launcher, depicted by the smooth angular velocity and acceleration profiles (2). As the flux-pinned interface draws the OSA in, some translational momentum transfers to angular momentum and oscillates about the equilibrium state (3). When the frame contacts the airplane hull, that external energy transfers and excites the OSA out of the potential well (4).

4. DYNAMIC METRICS

The dynamic state of interest for the rest of the paper is the sample cache's dynamic state relative to return vehicle in the return vehicle's frame, where state includes position $(r_x \, r_y \, r_z)$, attitude $(\theta_x \, \theta_y \, \theta_z)$, translational velocity $(v_x \, v_y \, v_z)$, and angular velocity $(\omega_x \, \omega_y \, \omega_z)$, in Eq. (1). The $x \, y \, z$ convention follows Figure 3.

$$\boldsymbol{s} = [x \;\; y \;\; z \;\; v_x \;\; v_y \;\; v_z \;\; \theta_x \;\; \theta_y \;\; \theta_z \;\; \omega_x \;\; \omega_y \;\; \omega_z] \qquad (1)$$

Each FPI docking design can be characterized by the following metrics:

1) maximum input energy resulting in successful capture,

2) contact/interaction imparted momentum change,

3) system damping (related to settling time), and

4) final system stiffness (related to deflections experienced given certain input disturbances).

All metrics forego analysis with any predictive dynamics model and are purely derived from sensor measurements collected during the experiments. Each metric is described in more detail in this section.

Maximum Input Energy/Bounds on Initial State for Capture

The relative dynamic state of the spacecraft prior to entering the flux-pinned interface's potential well determines the capture outcome for a given FPI design. Position and attitude dictate the alignment of the magnets with respect to the superconductors. This alignment determines the amount of attractive potential energy the system experiences when within the edge of the magnetic potential well. The translational velocity and angular velocity relate to the spacecraft's kinetic energy prior to entering the magnetic potential well. FPIs have a maximum input kinetic energy that result in capture of the system, related to the depth and shape of the potential well. If a system has more input energy than the FPI can absorb, the OS exits the potential well and does not successfully dock.

Metrics that identify bounds for each of these states that results in a successful capture are important. The FPI design may be more sensitive to certain states than others (for example, having less tolerance to translational velocity than angular velocity). Mapping the spacecraft's dynamic state to capture performance yields bounds of dynamic state to guarantee a successful capture.

Imparted Momentum Change at the Interface

Each spacecraft will experience a change in momentum as a result of an FPI interaction. Any interaction, contactless or non-contactless, transfers momentum and energy from one spacecraft body to the other spacecraft body. The amount the momentum is changed is dependent on the initial state of the system. For scenarios in which the spacecraft do not contact, the spacecraft experiences momentum change from the flux-pinning physics in a smooth and continuous manner. For scenarios in which initial momentum of the system cannot be arrested contactlessly, the system experiences a contact between the OSA-SROA system that imparts an impulsive change in momentum, which can cause damage to either spacecraft. Characterizing this momentum change allow FPI designers to evaluate input conditions that guarantee contactless interaction if necessary and ensure hardware tolerance to the interaction forces and torques. Additioanly, characterizing the momentum change allows a direct comparison of an FPI to a mechanical system that relies on these momentum changes during contact to bring the system to equilibrium.

System Damping

Once the FPI successfully executes a capture maneuver, the system settles towards its equilibrium state on a time scale determined by the system damping. A flux-pinned interface offers damping in the form of eddy current damping and hysteresis loss in the superconducting current vortices. Hysteresis loss is due to the magnetic field inhomogeneity and is manifested through thermal dissipation [26]. Eddy current damping is caused by the motion of magnets near a conductive surface and varies linearly with velocity [27]. Eddy current damping can be used to manage the input energy of a potential tumbling sample cache prior to any docking attempt near the aluminum structure of the return vehicle or to settle to equilibrium after a successful capture. Quantifying the total damping parameter characterizes the dissipation of energy and settling time of this underdamped oscillator, which shape the time scales of the capture operation.

Final Interface Stiffness at Equilibrium

Once captured, the spacecraft system oscillates within the confines of the magnetic potential well until all energy is dissipated through damping. The oscillations stem from a virtually rigid joint with nonlinear stiffness [28] [29] [17].

Although the concept of stiffness is well-documented and investigated for FPIs, each configuration is unique and must be specifically characterized. This metric is critical in understanding the magnetic potential well that governs the system's passive dynamics. The derivation from Eq. (2) to (5) illustrates an explicit relationship between stiffness and potential energy. $\Delta\boldsymbol{s}$ is the change in dynamic state of the orbiting spacecraft with respect to the equilibrium state, $\boldsymbol{s}_e$. $k(\boldsymbol{s})$ is the stiffness of the interface as a function of state. $\boldsymbol{F}$ is the force between the two spacecraft, following Hooke's law for a linearized spring. U is the potential energy as a function of state. For a general relationship between dynamic state to stiffness and potential energy, please refer to [11].

$$\boldsymbol{F} = k(\boldsymbol{s})\,\Delta\boldsymbol{s} \tag{2}$$

$$\boldsymbol{F} = \nabla U(\boldsymbol{s}) \tag{3}$$

$$k(\boldsymbol{s}_e)\Delta\boldsymbol{s} = \nabla U(\boldsymbol{s}_e) \tag{4}$$

$$k(\boldsymbol{s}_e) = \frac{\nabla U(\boldsymbol{s}_e)}{\partial \boldsymbol{s}} \tag{5}$$

The experimental results report the stiffness for each DOF at the equilibrium position and attitude. The oscillatory motion passes through or near equilibrium state at every period, thus the stiffness at this state generally represents the stiffness of the joint once the orbiting spacecraft is captured. Stiffness of the system will determine the frequency at which it oscillates and the deflections the system exhibits when exposed to disturbance forces or torques.

5. DYNAMICS CAPABILITIES

Maximum Input Energy/Bounds on Initial State for Capture

Over the 27 capture experiments conducted during microgravity, 15 experiments successfully captured and 12 did not capture on the time scales afforded by the experiment (~10 seconds). The outcome matrix with contact information for the 27 experiments is shown in Table 2, showing a breadth of capture outcomes used for analysis. During experimentation, the initial position of the OSA upon entering the flux pinning sphere of influence did not change. The initial attitude displacement from any equilibrium attitude varied by up to 72 degrees. Translational velocity and angular velocity varied within the bounds shown in Table 3, which shows that the set of experiments spanned the desired test range.

Table 2: Outcome matrix with capture success and contact information

Outcome Matrix Across 27 Experiments	Capture (Number of Trials)	No Capture (Number of Trials)
No Contact	8	3
Contact	7	9

Table 3: Bounds of OSA initial state across all capture experiments with desired capabilities

OSA Initial State	Imparted on Test System	Desired Test Capabilities
Translational Velocity [m/s]	[0.02 0.38]	[0.05 0.22]
Angular Velocity [rad/s]	[0.01 1.07]	[0.23 0.70]

The observed capture outcome for the test system is shown in Figure 9, in which the experiment OSA captures up to 0.25 m/s and 0.22 rad/s simultaneously. All trials below these values captured. When the translational velocity and angular velocity states are separately evaluated, the OSA captures up to 0.28 m/s and up to 1.068 rad/s. Of the 15 trials that captured, the range of initial conditions in the experiment set are listed in detail in Table 4 and Table 5.

Table 4: Bounds of OSA measured initial velocity across all capture experiments

	Measured Performance for the Test System		Estimated Performance for a Flight System		Required Range for Capture of a Flight System
Outcome as a Function of Translational Velocity	Capture	No Capture	Capture	No Capture	
No Contact [cm/s]	[1.7 22.3]	[18.0 22.9]	[0.7 10.0]	[8.1 10.3]	[2 10]
Contact [cm/s]	[11.1 28.5]	[12.7 38.3]	[4.9 12.7]	[5.7 17.1]	[2 10]

Table 5: Bounds of OSA measured initial angular velocity across all capture experiments

	Measured Performance for the Test System		Estimated Performance for a Flight System		Required Range for Capture of a Flight System
Outcome as a Function of Angular Velocity	Capture	No Capture	Capture	No Capture	
No Contact [RPM]	[1.2 10.2]	[2.7 5.0]	[0.5 4.6]	[1.2 2.2]	[1 3]
Contact [RPM]	[0.3 3.8]	[2.3 5.7]	[0.1 1.7]	[1.0 2.5]	[1 3]
No Contact [deg/s]	[7.2 61.2]	[16.0 29.8]	[3.2 27.4]	[7.1 13.3]	[6 18]
Contact [deg/s]	[1.6 22.9]	[13.9 34.0]	[0.7 10.2]	[6.2 15.2]	[6 18]

The estimates for a flight system are extrapolated from the data collected on the test system by scaling the mass of the OSA to match that of a notional OS while conserving energy. The extrapolated capture outcome for the 12.5 kg spaceflight OS is shown in Figure 10. When extended to a flight mass, this flux-pinned interface design can support the capture of a system where the OS is moving up to 0.11 m/s and 0.084 rad/s simultaneously relative to the SRO when contact dynamics are not in play. When the translational velocity and angular velocity states are separately evaluated, the OSA captures up to 0.13 m/s and up to 0.41 rad/s. 11 of 14 trials within the desired velocity bounds capture successfully but three trials did not capture at a low energy initial state within the desired capabilities range.

The duration of microgravity for one of these unsuccessful capture trials was not long enough for the system to allow capture past the initial interaction, although the system began to show restorative motion at the end of the trial, shown in Figure 11. There are two capture scenarios in which a contactless interaction from a low-energy state generates a no capture outcome. A closer study of this case should be conducted because it has clear implications for the efficacy of the flux-pinned system.

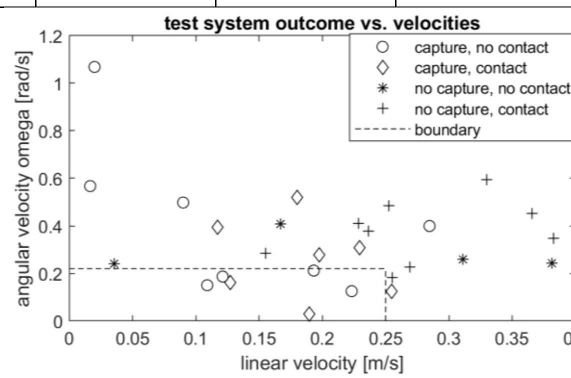

Figure 9: Observed capture outcome for test system

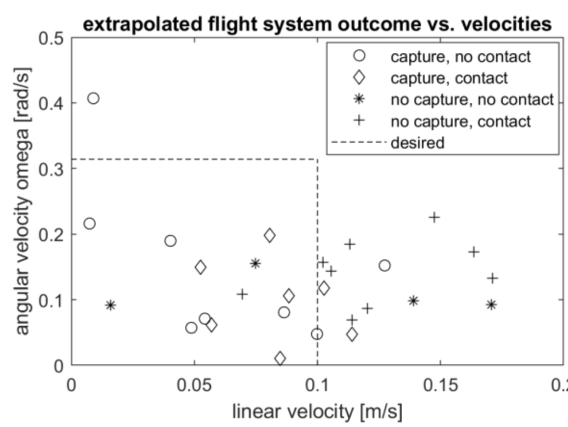

Figure 10: Most conservative, extrapolated capture outcome for spaceflight system

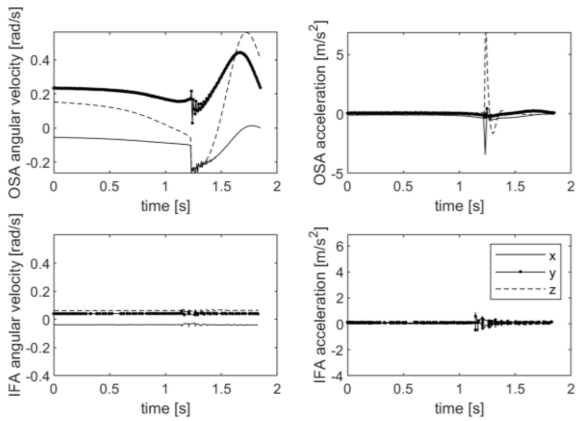

Figure 11: A trial in which the data implies restorative motion, but the experiment did not last long enough time to fully express capture

Total kinetic energy, T, is a more general metric to describe the docking interface's capabilities, shown in Eq. (6), where angular velocity is $\boldsymbol{\omega} = [\omega_x\ \omega_y\ \omega_z]$ and translational velocity is $\boldsymbol{v} = [v_x\ v_y\ v_z]$. Total kinetic energy, separated into capture outcomes, is depicted in Figure 12. Although components of energy are not depicted, rotational kinetic energy is significantly less than translational kinetic energy and constitutes up to 10% of the total energy of the system. Generally, lower total energy states are more likely to capture. From the wide distribution of energy states in each capture outcome, still there is not a clear direct mapping from energy to capture. To produce a comprehensive mapping, OSA attitude close to equilibrium must also be included in the mapping function.

$$T = \frac{1}{2} m \boldsymbol{v}^T \boldsymbol{v} + \frac{1}{2} \boldsymbol{\omega}^T I \boldsymbol{\omega} \qquad (6)$$

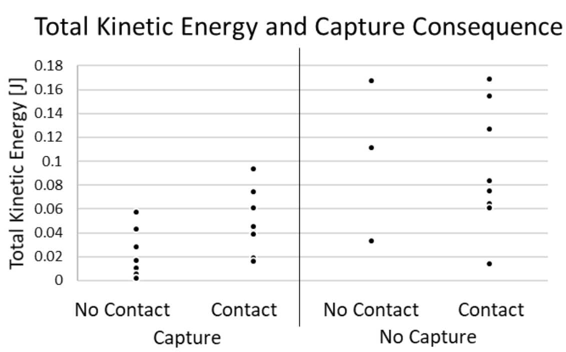

Figure 12: Total kinetic energy separated into capture and contact outcome

To complete the mapping function between state and capture outcome, position ($\boldsymbol{r} = [r_x\ r_y\ r_z]$) and attitude ($\boldsymbol{\theta} = [\theta_x\ \theta_y\ \theta_z]$) relates to potential energy with function f_U, seen in Eq. (7). Potential energy must be greater than kinetic energy to successfully capture, seen in Eq. (8), where $\delta_{capture}$ is 1 if a successful capture occurs and 0 otherwise. This task proves difficult as the potential energy is not directly observable and there currently does not exist an accurate analytical function mapping f_U. Instead, the kinetic energy measurements drive at discovering the depth and shape of the potential energy well indirectly by applying conservation of energy.

$$U = f_U(\boldsymbol{r}, \boldsymbol{\theta}) - f_U(\boldsymbol{r} = \infty) \qquad (7)$$

$$\delta_{capture} = \begin{Bmatrix} 1 & if\ U > T \\ 0 & if\ U < T \end{Bmatrix} \qquad (8)$$

Imparted Momentum Change at the Interface

Flux-pinned interfaces are distinct from other state-of-the-art capture systems because they increase the time over which the momentum exchange occurs between the two bodies. Without active control, FPIs eliminate or reduce the impulsive exchange characteristic of mechanical contact in a docking system. For the capture experiments, the first contact upon entering the magnetic potential well measured forces up to 120 N whereas the first contactless interaction upon entrance measured forces up to 20 N, seen in Figure 13. The integrated momentum change across the entire time scale of the contactless interaction is comparable to the trials that contacted.

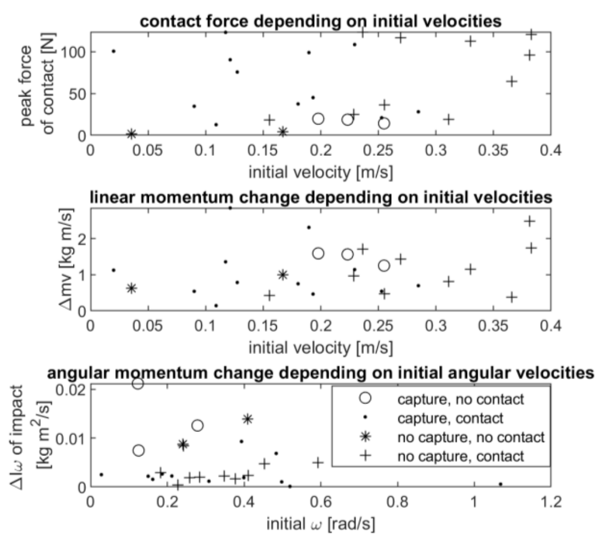

Figure 13: Contact force and angular momentum change with respect to initial velocities

Characteristics of momentum exchange and peak force are functions of the initial dynamic state and show trends with the resultant capture outcome, seen visually in Figure 13 and qualitatively in Table 6. The trends are specific to the experiments observed, with sample sizes explicitly stated under each classification in Table 6. The bounds in initial dynamic states are binned by capture outcome. For the ideal outcome of capturing without contact, the initial state held mid-range velocity and low-range angular velocity, which resulted in low peak force and mid to high exchange in both linear and angular momentum. For a successful capture with contact, the initial translational velocity ranges from low to mid energetic level whereas the angular velocity ranges the entire spectrum, as capture outcome is more sensitive to translational velocity. The resultant peak force also varies from glancing contacts to high energy dissipating contacts, which reflects the linear momentum variance, but angular momentum exchange consistently remains minimal. The trials that did not capture contactlessly reflect similarities between the trials that did capture contactlessly. The initial states have low energy, but the difference is more allocation into initial angular velocity. For the least ideal outcome of not capturing upon first attempt and contacting, the subsequent interaction is very similar to the trials that did capture with contact but differ consistently in having more energetic initial states. Some of the variability in the results are a function of the difference in potential energy in the system caused by different initial attitudes.

Table 6: Different capture outcomes with initial velocities, peak force, and momenta exchange characterized with numerical ranges and qualitative ranges

	v_0 [m/s]	ω_0 [rad/s]	Peak Force [N]	Δmv [kg·m/s]	$\Delta I\omega$ [kg·m^2/s] ×10^{-3}
Capture No Contact [n = 8]	[0.20 0.25] Mid	[0.12 0.28] Low	[14 20] Low	[1.3 1.6] Mid	[7.5 21] Mid - High
Capture Contact [n = 8]	[0.02 0.28] Low - Mid	[0.03 1.06] Low - High	[13 120] Low - High	[0.1 2.8] Low - High	[0.1 9.3] Low
No Capture No Contact [n = 3]	[0.036 0.17] Low	[0.24 0.40] Mid	[2 4.3] Low	[0.6 1] Low	[9 14] Mid - High
No Capture Contact [n = 9]	[0.16 0.38] Mid - High	[0.17 0.59] Mid - High	[18 123] Low - High	[0.37 2.5] Low - High	[0.4 8.5] Low - Mid

System Energy Damping Parameter

Once the system successfully captures, damping removes energy from the OSA until it settles to its equilibrium position and attitude. To clearly observe the damping effects, the OSA was placed near equilibrium for 23 experiments. The longest trial lasted up to 9 seconds and the shortest, 2 seconds. The average trial lasted 4 seconds. Damping is visible in all the successfully captured experiments but especially visible in equilibrium data, seen in Figure 14. The damping parameter discussed in this section is derived from only the equilibrium tests because the capture tests do not present enough underdamped oscillations in each trial and show nonlinear dynamics.

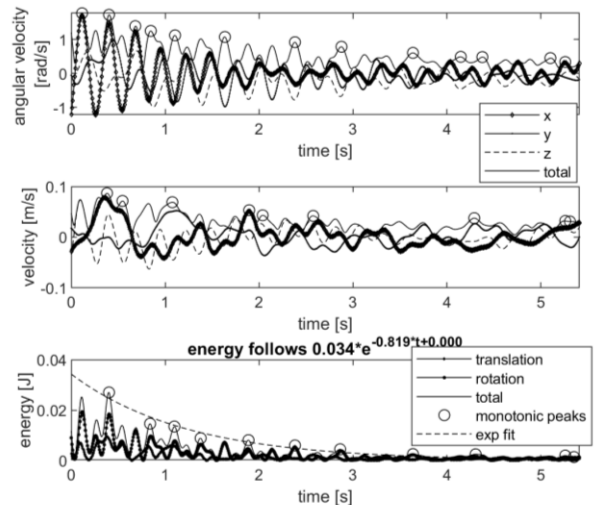

Figure 14: Sample IMU data from a single equilibrium trial, showing angular velocity, translational velocity, and energy with exponential fit

The two spacecraft bodies start very close to equilibrium and with small perturbations, where the nonlinear dynamics can be approximated as locally linear. The dynamics are coupled in all six degrees of freedom, which lead to coupling of damping and mass parameters between translational and rotational states. For simplicity, the damping parameter discussed here describes the dissipation of total kinetic energy over time, depicted in Figure 15. Total system kinetic energy absorbs the differing mass and state-dependent damping terms into one state over time. This damping term is specific to the current configuration and lacks generality to other flux-pinned interfaces but may offer an approximation for similar magnet-superconductor systems.

$$E(t) = Ae^{-\gamma t}\cos(\omega_d t + \phi) \quad (9)$$

While FPIs inherently represent nonlinear dynamics, framing FPI behavior with a linear approximation is convenient. By assuming linear damping and stiffness, the underdamped oscillations are represented by Eq. (9). $E(t)$ is the system energy over time. γ is a combination of damping coefficients and mass/inertia in all degrees of freedom that encapsulates total energy dissipation. $A, \omega_d,$ and ϕ, are constants specific to the configuration: amplitude response, damped frequency, and phase shift. Across the 23 equilibrium experiments, the best estimates of γ and its distribution are reported in Table 7 and Figure 15. The distribution of γ is skewed to smaller values, as the median value is significantly smaller than the mean value. The small normalized root mean square error shows that the exponential fit with a linear damping relationship is a good fit and consistent within each experiment trial.

The wide distribution spread demonstrates that the damping parameter is inconsistent across all trials, illustrating that the damping depends on the system state. $1/\gamma$ is the time constant, τ_s, defining settling time of the system. The settling time to reach 2% of the initial energy state is listed in Table 7. The values in Table 7 represent estimates of wait time before moving onto the next operational phase.

Table 7: Characteristics of damping estimate distribution

	$\gamma \equiv 1/\tau_s$	2% settling time [s]
$E[\cdot]$	0.7355	7.06
$\sigma(\cdot)$	0.36	4.12
median	0.6815	5.87

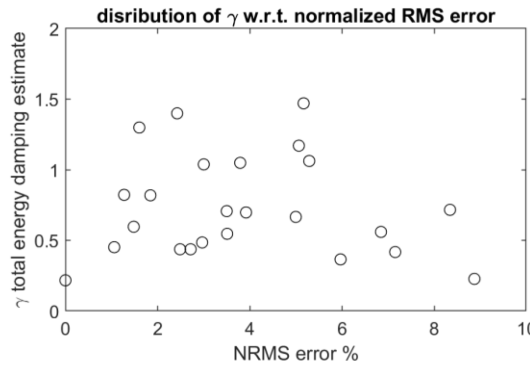

Figure 15: Damping estimate and associated normalized RMS error

System Damping and Stiffness in Each DOF

Deriving a stiffness value about the equilibrium provides insight into general dynamic behavior, such as natural frequencies. The stiffness of the interface changes with the direction and magnitude of the motion about the equilibrium – especially in motions normal to the face of the superconductors. The damping in each degree of freedom describes the dissipation of each state and differs from the previous section, which analyzes system energy damping.

A linearized state transition matrix that incorporates stiffness and damping matrices is shown in Eq. (10). K represents the stiffness matrix that is positive definite and C represents the damping matrix populated by nonnegative values along the diagonal. Δt is the time difference between the previous measurement and the next measurement, constant if the sensor samples uniformly. 1_3 are identity matrices of size 3 along each dimension and 0_3 is analogously a square matrix of zeros of dimension 3.

$$\begin{bmatrix} \boldsymbol{r} \\ \boldsymbol{\theta} \\ \boldsymbol{v} \\ \boldsymbol{\omega} \end{bmatrix}_{k+1} = \begin{bmatrix} 1_3 & 0_3 & \Delta t 1_3 & 0_3 \\ 0_3 & 1_3 & 0_3 & \Delta t 1_3 \\ -\frac{K_{rr}\Delta t}{M} & \frac{-K_{r\theta}\Delta t}{I} & 1_3 - \frac{C_{rr}\Delta t}{M} & 0_3 \\ -\frac{K_{\theta r}\Delta t}{M} & -\frac{K_{\theta\theta}\Delta t}{I} & 0_3 & 1_3 - \frac{C_{\theta\theta}\Delta t}{I} \end{bmatrix} \begin{bmatrix} \boldsymbol{r} \\ \boldsymbol{\theta} \\ \boldsymbol{v} \\ \boldsymbol{\omega} \end{bmatrix}_{k} \tag{10}$$

By utilizing IMU-generated velocity measurements, the K and C values that minimize error between propagated state and measured state are computed with the CVX convex optimizer. The positive definite and nonnegative constraints are encoded into this optimization. The state matrix assumes a linear propagation of stiffness and damping, an accurate assumption for states close to equilibria. The resulting linear relationship fits well; a sample of data shown in Figure 16 in which the measurements and propagated states are nearly indistinguishable. All state predictions fit within 2.5% normalized root mean squared error.

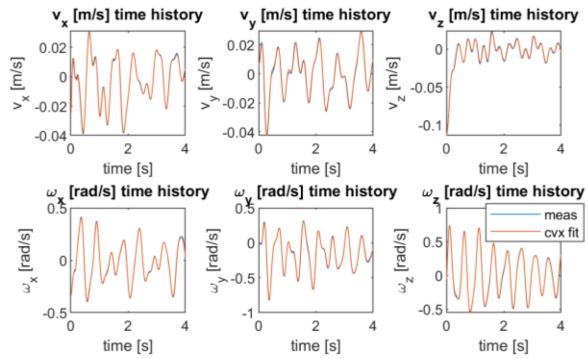

Figure 16: Comparison of measured and propagated velocity state from one experiment, fit with linear stiffness and damping

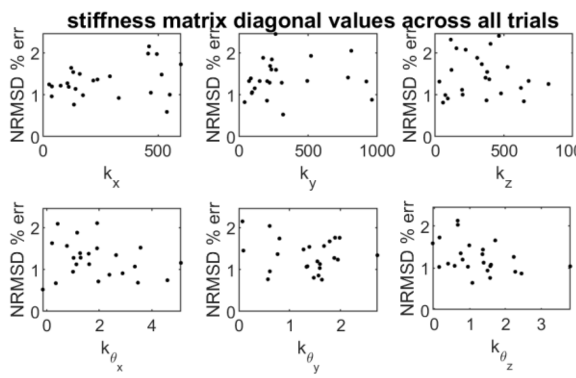

Figure 17: Stiffness matrix diagonal values across trials

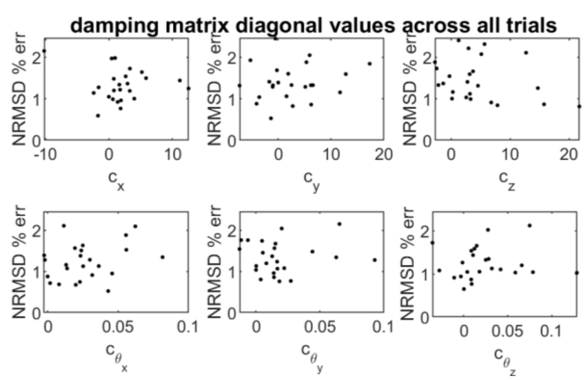

Figure 18: Damping matrix diagonal values across trials

The stiffness and damping parameters from all the trials plotted against the normalized root mean squared deviation (NRMSD) percent error are shown in Figure 18 and Figure 18. The distribution characteristics of stiffness and damping are listed in

Table **8** and Table 9. The standard deviation for each of the stiffness and damping values are nearly as large as the expected value, revealing the inconsistency from trial to trial. Just like the energy analysis, the distribution spread demonstrates that the stiffness and damping parameters are consistent within a trial and inconsistent across all trials. There is a relationship to initial state that is needed to fully describe the anticipated stiffness and damping.

Table 8: Stiffness values resulting from discrete state matrix fit

	K_x	K_y	K_z	K_{θ_x}	K_{θ_y}	K_{θ_z}
$E[\cdot]_{meas}$	554	262	108	1.57	0.92	0.88
$\sigma[\cdot]_{meas}$	265	176	109	1.34	0.81	0.73
median	524	192	73	1.53	0.52	0.69

Table 9: Damping values resulting from discrete state matrix fit

	C_x	C_y	C_z	C_{θ_x}	C_{θ_y}	C_{θ_z}
$E[\cdot]_{meas}$	2.63	3.58	4.93	0.027	0.020	0.027
$\sigma[\cdot]_{meas}$	3.29	4.77	5.80	0.021	0.024	0.033
median	1.71	1.72	3.17	0.024	0.014	0.014
2 % settling time ($E[C_s]$)	1.11	0.82	0.44	75	108	84

The damping parameter is magnitudes greater in the translational degrees of freedom than the rotational degrees of freedom. The position states take less than 2 seconds to settle within 2% of the initial state but the rotational modes take up to 2 minutes to damp out. The difference in translational vs rotational dissipation is clearly visible in the equilibrium tests. All trials lasted long enough to see the translational states settle but not long enough to observe the rotational modes settle significantly.

Summary

The individual metrics that characterize the FPI describe the dynamic behavior throughout the entire docking maneuver. Initiating the capture operation to successfully capture, the flight system OS enters the magnetic potential well with relative motion up to 0.11 m/s and 0.084 rad/s simultaneously. Upon successful capture, the OS experiences a peak force of either an impulsive contact, up to 120 N, or a contactless momentum exchange, up to 20 N. The total system kinetic energy dissipates to within 2% of initial magnitude within ~ 12 seconds. The system settles into equilibrium through underdamped oscillations, characterized by translational stiffness of 100 – 550 N·m and angular stiffness of 0.9 – 1.6 N·m. The last DOF to settle to within 2% of initial value is rotation about $\hat{\boldsymbol{y}}$, which settles after ~ 2 minutes. After the slowest mode dissipates, the docking maneuver is complete.

6. CONCLUSIONS

Discussion

A conceptual Mars Sample Return mission motivates the technology development a flux-pinned interface to perform docking and capture. The design of the experiment analogues is similar in mass and geometry of the mission concept and the experiment campaign reflects the initial conditions that the spacecraft would experience in spaceflight operations. The microgravity experiment campaign aimed at characterizing the capabilities of this system in five different dynamical metrics, such as energetic states to successfully capture, momentum exchange, rate of energy dissipation, and stiffness. This body of work matures and characterizes flux-pinning technology for consideration in the MSR concept but also aims to inform future technologists who wish to utilize flux-pinned interfaces for other use cases.

As designed and implemented in the experiments described in this work, this flux-pinned interface does not meet the desired capabilities specified by the most conservative MSR requirements. With a less stringent spaceflight OS mass requirement of 4.3 kg, the desired capability to successfully capture fulfills the initial velocity specifications. The observed performance of the OSA is farther from fulfilling the angular velocity requirement given that the entrance attitude may be any orientation. If the entrance attitude is specified within smaller bounds, the FPI can produce better performance.

Upon successful capture, the reported damping parameters bound the settling time to under 2 minutes. After sufficient settling time, the OS is in equilibrium and remains in equilibrium with a certain stiffness. The stiffness of the interface offers two insights: the maximum external disturbance the FPI can tolerate and maintain the FPI with the OS and the necessary work required to detach the OS from the SRO. The stiffness values reported in the results are the expected spaceflight stiffness values if the magnetic image remains identical. Although the characterization is limited in the amount of states measured, these metrics represent approximate values. Either more testing is needed to empirically observe all states of interest or a more predictive, higher fidelity dynamics model must be developed to simulate states of interest.

FPIs are contactless, passive, and stabilizing but there are definitive limitations to these qualities. This paper aims to quantify the performance of FPIs for a sample return mission. The capture mechanism demonstrates capabilities that are not offered by conventional mechanisms at this mass and power specification. Additionally, flux-pinning offers unique advantages that should be considered for specific applications but these limitations must be understood and designed around.

Future Work

Although the results revealed general insights into each metric, further work involves refining every mapping function by incorporating position and attitude information if applicable. The capture outcome boundary is unclear with only the velocity states, but by incorporating the position and attitude information, a boundary may be distinguished. By including attitude misalignment upon entrance, a boundary could be found to guarantee contactless interactions. For the stiffness and damping analysis, the IMU measurements shall be transformed into the SROA relative frame as the OSA body measurements do not yield precise interface characteristics. As this paper addresses system level metrics, a large body of work remains in producing a predictable dynamics model from the same data set.

ACKNOWLEDGEMENTS

F. Zhu thanks the NASA Space Technology Research Fellowship Grant NNX15AP55H for supporting this research.

The research was carried out at the Jet Propulsion Laboratory, California Institute of Technology, under a contract with the National Aeronautics and Space Administration.

REFERENCES

[1] J. P. Shoer and M. A. Peck, "Flux-Pinned Interfaces for the Assembly, Manipulation, and Reconfiguration of Modular Space Systems," *J of Astronaut Sci*, vol. 57, no. 3, pp. 667–688, Jul. 2009.

[2] J. Shoer and M. Peck, "A Flux-Pinned Magnet-Superconductor Pair for Close-Proximity Station Keeping and Self-Assembly of Spacecraft," in *AIAA Guidance, Navigation and Control Conference and Exhibit*, Hilton Head, South Carolina, 2007.

[3] J. Shoer and M. Peck, "Reconfigurable Spacecraft as Kinematic Mechanisms Based on Flux-Pinning Interactions | Journal of Spacecraft and Rockets," *Journal of Spacecraft and Rockets*, vol. 46, no. 2, pp. 466–469, 2009.

[4] F. Zhu, L. Jones-Wilson, and M. Peck, "Capturing and Docking Spacecraft with Flux-Pinned Interfaces," presented at the International Astronautical Congress, Guadalajara, Mexico, 2016.

[5] R. P. Kornfeld, J. C. Parrish, and S. Sell, "Mars Sample Return: Testing the Last Meter of Rendezvous and Sample Capture," *Journal of Spacecraft and Rockets*, vol. 44, no. 3, pp. 692–702, 2007.

[6] E. H. Brandt, "Rigid levitation and suspension of high-temperature superconductors by magnets," *American Journal of Physics*, vol. 58, no. 1, pp. 43–49, Jan. 1990.

[7] L. C. Davis, E. M. Logothetis, and R. E. Soltis, "Stability of magnets levitated above superconductors," *Journal of Applied Physics*, vol. 64, no. 8, pp. 4212–4218, Oct. 1988.

[8] L. Jones and M. Peck, "Stability and Control of a Flux-Pinned Docking Interface for Spacecraft," in *AIAA Guidance, Navigation, and Control Conference*, American Institute of Aeronautics and Astronautics.

[9] L. Jones and M. Peck, "Control Strategies Utilizing the Physics of Flux-Pinned Interfaces for Spacecraft," in *AIAA Guidance, Navigation, and Control Conference*, American Institute of Aeronautics and Astronautics.

[10] L. Jones, W. Wilson, and M. Peck, "Design Parameters and Validation for a Non-Contacting Flux-Pinned Docking Interface," in *AIAA SPACE 2010 Conference & Exposition*, American Institute of Aeronautics and Astronautics.

[11] F. Zhu, L. Jones-Wilson, and M. Peck, "Flux-Pinned Dynamics Model Parameterization and Sensitivity Study," presented at the IEEE Aerospace Conference, Big Sky, Montana, 2018.

[12] M. C. Sorgenfrei, L. L. Jones, S. S. Joshi, and M. A. Peck, "Testbed Validation of Location-Scheduled Control of a Reconfigurable Flux-Pinned Spacecraft Formation," *Journal of Spacecraft and Rockets*, vol. 50, no. 6, pp. 1235–1247, 2013.

[13] W. Wilson, L. Jones, and M. Peck, "A Multimodule Planar Air Bearing Testbed for CubeSat-Scale Spacecraft," *Journal of Dynamic Systems, Measurement and Control*, vol. 135, no. 4, 2013.

[14] J. Shoer, W. Wilson, L. Jones, M. Knobel, and M. Peck, "Microgravity Demonstrations of Flux Pinning for Station-Keeping and Reconfiguration of CubeSat-Sized Spacecraft | Journal of Spacecraft and Rockets," *Journal of Spacecraft and Rockets*, vol. 47, no. 6, pp. 1066–1069, 2010.

[15] L. Jones, W. Wilson, J. Gorsuch, J. Shoer, and M. Peck, "Flight Validation of a Multi-Degree-of-Freedom Flux-Pinning Spacecraft Model," in *AIAA Guidance, Navigation, and Control Conference*, Portland, Oregon, 2011.

[16] R. Williams and J. R. Matey, "Equilibrium of a magnet floating above a superconducting disk," *Appl. Phys. Lett.*, vol. 52, no. 9, pp. 751–753, Feb. 1988.

[17] F. Zhu and M. Peck, "Linearized Dynamics of General Flux-Pinned Interfaces," *IEEE Transactions on Applied Superconductivity*, vol. 28, no. 8, pp. 1–10, Dec. 2018.

[18] A. A. Kordyuk, "Magnetic levitation for hard superconductors," *Journal of Applied Physics*, vol. 83, no. 1, pp. 610–612, Jan. 1998.

[19] P. B. Landecker, D. D. Villani, and K. W. Yung, "An Analytic Solution for the Torque Between Two Magnetic Dipoles," *Physical Separation in Science and Engineering*, 1999.

[20] K. W. Yung, P. B. Landecker, and D. D. Villani, "An Analytic Solution for the Force Between Two Magnetic Dipoles," *Physical Separation in Science and*

Engineering, 1998.
[21] P. Younse, J. Strable, M. Dolci, P. Ohta, K. Lalla, and E. Olds, “An Orbiting Sample Capture and Orientation System Architecture for Potential Mars Sample Return,” presented at the IEEE Aerospace 2018, Big Sky, Montana, 2018.
[22] P. Younse *et al.*, “A Flux-Pinning Concept for On-orbit Capture and Orientation of an MSR Orbiting Sample Container,” presented at the IEEE Aerospace Conference, Big Sky, MT, 2019.
[23] I. McKinley, C. Hummel, and J.-W. Jones-Wilson Laura, “A Flight-Traceable Cryogenic Thermal System for Use in a Sample-Capture Flux-Pinned Interface,” presented at the IEEE Aerospace 2019, Big Sky, Montana, 2019.
[24] E. Olson, “AprilTag: A robust and flexible visual fiducial system,” in *2011 IEEE International Conference on Robotics and Automation*, 2011, pp. 3400–3407.
[25] “Levitation bulk,” *CAN SUPERCONDUCTORS*. [Online]. Available: http://www.can-superconductors.com/levitation-bulk.html. [Accessed: 04-Feb-2018].
[26] Y. Sakurai, T. Matsumura, H. Kataza, S. Utsunomiya, and R. Yamamoto, “Estimation of the Heat Dissipation and the Rotor Temperature of Superconducting Magnetic Bearing Below 10 K,” *IEEE Transactions on Applied Superconductivity*, vol. 27, no. 4, pp. 1–4, Jun. 2017.
[27] “(4) Magnetic braking: Simple theory and experiment | Request PDF,” *ResearchGate*. [Online]. Available: https://www.researchgate.net/publication/252850785_Magnetic_braking_Simple_theory_and_experiment. [Accessed: 07-Sep-2018].
[28] Y. Lu, M. Zhang, and D. Gao, “Connection stiffness and dynamical docking process of flux-pinned spacecraft modules,” *Journal of Applied Physics*, vol. 115, no. 6, p. 063904, Feb. 2014.
[29] J. Shoer and M. Peck, “Stiffness Of A Flux-Pinned Virtual Structure For Modular Spacecraft,” *Journal of the British Interplanetary Society*, vol. 62, pp. 57–65, 2009.

BIOGRAPHY

Frances Zhu *earned her B.S. in Mechanical and Aerospace Engineering from Cornell University, Ithaca in 2014 and is currently pursuing a Ph.D. in Aerospace Engineering at Cornell. Since 2014, she has been a Research Assistant with the Space Systems Design Studio, specializing in dynamics, systems, and controls engineering. Her research interests include flux-pinned interface applications, spacecraft system architectures, robot dynamics, estimation, and controls. Ms. Zhu is a NASA Space Technology Research Fellow.*

Mitchell Dominguez *earned his B.S. in Mechanical and Aerospace Engineering from Cornell University in 2018 and is currently pursuing a M.Eng. in Aerospace Engineering at Cornell. He has been a Research Assistant with the Space Systems Design Studio since 2014, working on dynamics, computer vision, and mechanical design. Mitchell's research interests include flux-pinned interfaces, spacecraft systems, and dynamics and controls of autonomous robots.*

Mason A. Peck *earned a B.S. in Aerospace Engineering from the University of Texas at Austin. He worked at Bell Helicopter from 1993 to 1994 on structural dynamics. From 1994 to 2001 he was an attitude dynamics specialist and systems engineer at Hughes Space and Communications (now Boeing Satellite Systems). During his years at Boeing he served as attitude dynamics lead in the Boeing mission control center, participating in real-time spacecraft operations and helping to resolve spacecraft performance anomalies. He earned his M.S. and Ph.D. at UCLA as a Howard Hughes Fellow from 1998 to 2001. In 2001 he joined Honeywell Defense and Space Systems, and in 2003 was named Principal Fellow. He has been issued several patents. In July of 2004, he joined the faculty at Cornell University, where he teaches courses in dynamics and control and in the mechanical and aerospace engineering program. He was promoted to Associate Professor in fall 2010. In 2012, he was appointed as NASA's Chief Technologist.*

Laura Jones-Wilson *earned her Bachelor of Science in aerospace engineering with a minor in mathematics in 2007. Laura graduated in the summer of 2012 with her Ph.D. in Aerospace Engineering, with a concentration in Dynamics and Controls and a minor in Astronomy. She was awarded both the National Science Foundation (NSF) Graduate and the National Defense Science and Engineering Graduate (NDSEG) Fellowship. Presently, Dr. Jones-Wilson is a Guidance and Control Systems Engineer at NASA Jet Propulsion Laboratory.*